A 25-μW All-MOS Potentiostatic Delta-Sigma ADC for Smart Electrochemical Sensors

Stepan Sutula, *Student, IEEE,* Jofre Pallarès, Javier Gonzalo-Ruiz, Francesc Xavier Muñoz-Pascual, Lluís Terés, and Francisco Serra-Graells, *Member, IEEE*

***Abstract*—This paper presents a low-power all-MOS delta-sigma ADC specifically optimized for the potentiostatic biasing and amperometric read-out of electrochemical sensors. The proposed architecture reuses the dynamic properties of the sensor itself to implement a continuous-time mixed electrochemical delta-sigma modulator with minimalist analog circuits fully integrable in purely digital CMOS technologies. A 25-μW smart electrochemical sensor demonstrator integrated in low-cost 1M CMOS technology with Au post-processing is presented. Experimental results show electrical dynamic range values exceeding 10-bit, while electrochemical figures exhibit linearity levels close to R^2=0.999 combined with RSD<15% in terms of reproducibility. A comparative test with commercial potentiostat equipment is also included to qualify the performance of the proposed ADC.**

***Index Terms*—Low-power, CMOS, all-MOS, delta-sigma, modulation, analog-to-digital, conversion, potentiostat, amperometric, read-out, electrochemical, smart sensors.**

I. Introduction

SMART sensor networks are probably one of the most clear examples of the so-called ubiquitous computing [1]. In this scenario, a large number of ultra low-power, compact and low-cost sensing nodes are capable of capturing signals from their surrounding world, processing them locally to extract the desired information, and communicating the resulting data to a remote receiver through a distributed network. Nowadays, smart sensors are becoming the core technologies of a wide variety of promising applications, ranging from medical devices in body area networks (BANs) [2] to flexible tags for monitoring the quality of perishable food along its supply chain [3].

Despite the intrinsic limitations in terms of speed, lifetime and packaging costs, the interest in integrated chemical sensors has recently grown due to their inherent facility to interact with living organisms at microscopic scale [4], and also to the possibility of increasing sensor selectivity by the functionalization of its surface to detect a particular chemical compound [5]. In particular, electrochemical sensors are gaining positions thanks to their simple structure, typically reduced to a set of reference (R), working (W) and counter (C) planar microelectrodes, which makes them suitable for CMOS integration [6], [7]. However, electrochemical sensor performance is not only driven by microelectrode geometry and material, but also by its electrical operating conditions. In fact, this type of chemical sensors requires a potentiostatic biasing control to ensure that no current is flowing through terminal R and the differential voltage between terminals R and W is kept at a static potential. Under these operating conditions, the sensor signal can be then read-out as the measurement of the current flowing through terminals C and W. Thus, the CMOS smart front-end for an electrochemical sensor must include not only the analog-to-digital converter (ADC), but also the proper potentiostat and amperometric read-out circuits.

Figure 1(a) shows the classic circuit implementation for this smart front-end [7]–[9]. The purpose of the voltage follower OA2 is to avoid any current flowing through terminal R, while OA1 is in charge of keeping the potential of this terminal to the desired DC voltage V_{ref}. An extra current-to-voltage converter OA3 is also needed here to translate the amperometric read-out (I_{sens}) to an equivalent voltage signal (V_{sens}) before being converted to the digital domain (d_{sens}) by the ADC stage. Since OA3 is already forcing a virtual ground in terminal W, the differential voltage between reference and working microelectrodes (V_{rw}) is effectively biased at the static potential V_{ref}. Unfortunately, the multi-OpAmp potentiostat and amperometric stage together with the generic ADC of Figure 1(a) may demand power figures easily exceeding the acceptable target for smart sensor networks. Furthermore, the CMOS process options and area requirements for the integration of the resistors can also result in excessive fabrication costs.

In practice, the more compact and specific front-end architecture of Figure 1(b) is commonly employed [10]–[18]. In this case, potentiostat and amperometer functions are achieved by combining the voltage control loop supplied by OA1 with the current monitoring capability of mirror M1-M2 [19]. Hence, the behavior of the first stage is somehow similar to a current-conveyor [20]. The resulting signal I_{sens} is then directly A/D converted through time-domain processing techniques such as current-to-frequency (I/F) conversion [10], [15], [17], [18] or delta-sigma modulation [12], [14]. Finally, low-pass digital filtering is usually applied to scale the sampling frequency down to the Nyquist rate. Even with the overall circuit reduction compared to Figure 1(a), the front-end architecture of Figure 1(b) may still exhibit power and area figures exceeding those from the electrochemical sensor itself. This fact can be critical in emerging ultra low-power and low-cost smart sensor networks.

This paper addresses all the above issues by proposing

S. Sutula, J. Pallarès, J. Gonzalo-Ruiz, F. X. Muñoz-Pascual, L. Terés and F. Serra-Graells are with Instituto de Microelectrónica de Barcelona IMB-CNM(CSIC), Spain (e-mail:paco.serra@imb-cnm.csic.es).

F. X. Muñoz-Pascual is also with MATGAS A.I.E., Spain.

F. Serra-Graells is also with Universitat Autònoma de Barcelona, Spain.

(c) 2014 IEEE. Personal use of this material is permitted. Permission from IEEE must be obtained for all other users, including reprinting/ republishing this material for advertising or promotional purposes, creating new collective works for resale or redistribution to servers or lists, or reuse of any copyrighted components of this work in other works. http://dx.doi.org/10.1109/TCSI.2013.2284179

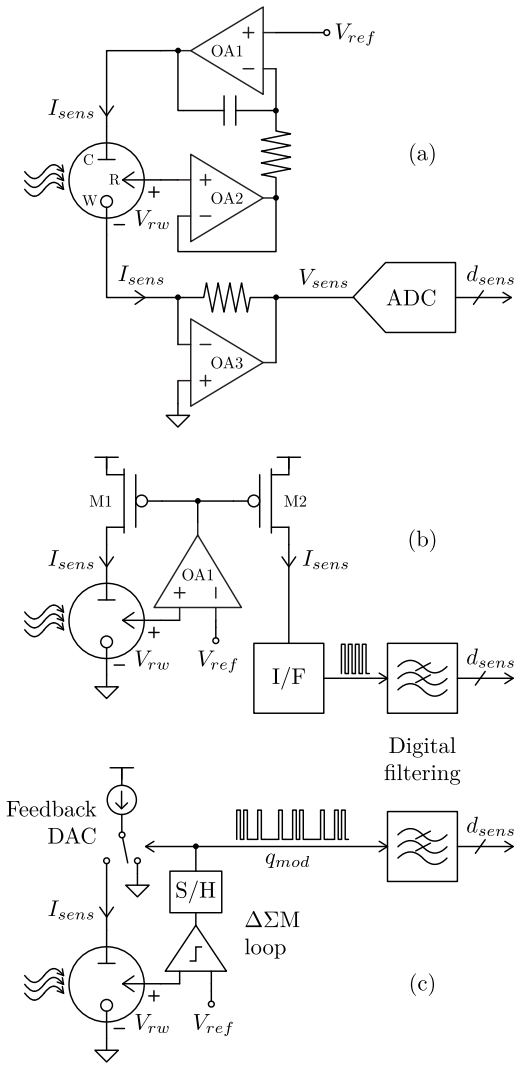

Figure 1. Classic (a), current-conveyor like (b) and proposed ΔΣM (c) potentiostat architectures for the amperometric digital read-out of electrochemical sensors.

the alternative front-end architecture of Figure 1(c). Basically, the idea is to take advantage of the typical long time constant of electrochemical sensors [21] to avoid large on-chip capacitors in a circuit-minimalist delta-sigma modulator (ΔΣM) interface. In particular, the mixed electrochemical ΔΣM loop reuses the sensor time-constant in the chemical domain to implement a continuous-time (CT) first-order noise shaper. The rest of ΔΣM blocks, which are the single-bit quantizer, the sample-and-hold and the feedback digital-to-analog converter (DAC), can be then easily realized in the electronic domain using ultra low-power and all-MOS circuits like a latched comparator, a flip-flop and a switched-current source, respectively. Thanks to the closed loop operation of the ΔΣM, the potentiostat function is inherently executed by the quantizer, which tends to keep V_{rw} at the desired static potential V_{ref}. Concerning the amperometric read-out of I_{sens}, its digitally modulated representation is already available at the input of the feedback DAC, that is at the output of the ΔΣM (q_{mod}). Hence, the low-pass digital filtering of the output stream completes the A/D conversion, and it scales the sampling frequency down to the Nyquist rate.

Compared to the previous architectures, the electrochemical sensor font-end proposed here only needs a minimalist analog circuitry, so it can be designed to achieve both static power consumption and integration area values comparable to the sensor alone. Furthermore, its circuit implementation does not require any special process option so it can be integrated in a purely digital CMOS technology, which makes it suitable for low-cost network applications as well. To the authors knowledge, the only comparable front-end architecture for electrochemical sensors is found in [22]. However, the resulting circuit in that case needs to be integrated in a mixed-signal CMOS technology with capacitor process options available, showing higher integration costs. Also, due to its low-impedance DAC, the feedback current waveform is more dependent on the non-linear sensor impedance, which may turn into the well-known waveform asymmetry issues of CT ΔΣMs [23].

The present paper is organized as follows. Section II introduces the equivalent circuit used to describe the dynamics of the electrochemical sensor. Based on this electrical model, Section III analyzes the operation of the proposed electrochemical ΔΣM architecture from the signal processing viewpoint. The ultra low-power and all-MOS circuits selected to complete the electronic part of the ΔΣM are introduced in Section IV. Taking into account all these proposals, a smart electrochemical sensor demonstrator fully integrated in a low-cost 1M CMOS technology is presented in Section V. The experimental results obtained from the electrical and electrochemical tests of this smart sensor are reported in Section VI. Finally, conclusions are summarized in Section VII.

II. Electrochemical Sensor Modeling

Since the ΔΣM proposed in Figure 1(c) reuses the dynamic properties of the electrochemical sensor to implement the noise shaping function, the accurate modeling of this type of sensors is required. For this purpose, the three-terminal symbol for electrochemical sensors is depicted in Figure 2(a), where the reference (R), working (W) and counter (C) microelectrodes can be easily identified. Under the potentiostatic operation described in the previous section, the sensor shows the non-linear electrical impedance model of Figure 2(b) [24], which is decomposed into the counter microelectrode (R_{ctc} and C_{dlc}), the solution between the three microelectrodes (R_s), and the working microelectrode (R_{ctw} and C_{dlw}). In this model, $R_{ctc|w}$ stand for the charge-transfer resistances, $C_{dlc|w}$ are the so-called double layer capacitances of the electrode-solution interfaces, and R_s is the electrolyte solution resistance.

Some considerations can be argued at this point to simplify the full impedance model of Figure 2(b). Firstly, solution resistance values are usually some orders of magnitude lower than the charge-transfer resistance counterparts, which are typically around several hundreds of kΩ. In this sense, experimental impedance measurements performed on integrated electrochemical sensors similar to the demonstrator of Section V using Autolab PGSTAT302N potentiostat coupled with Eco Chemie FRA32M impedance analysis module report R_s

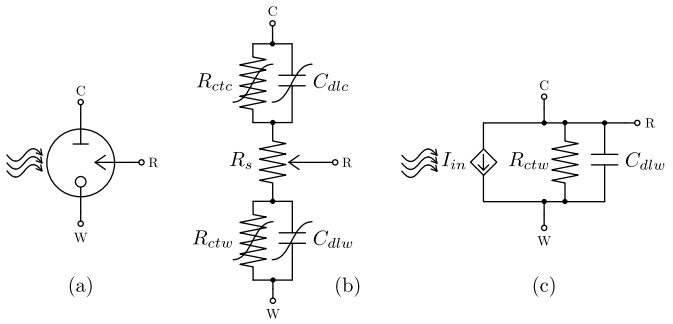

Figure 2. Symbol (a), non-linear electrical impedance model (b) and linearized equivalent circuit (c) for the electrochemical sensor of Figure 1.

values ranging from 200Ω to 1kΩ, depending on the electrolyte solution. Secondly, comparative measurements between the electrochemical sensor cell with internal (micro) or external (macro) counter electrodes show no significant differences in terms of electrical impedance, suggesting the counter microelectrode impedance value is lower than the working one, thus this part can be also neglected in practice. As a result, the equivalent linear circuit for electrochemical sensors is simplified to Figure 2(c), where I_{in} stands for the current change caused by the sensor impedance variation due to the chemical transduction.

III. Electrochemical Delta-Sigma Modulator Architecture

Figure 3(a) shows the circuit architecture of the proposed electrochemical ΔΣM, where I_{FS} and ϕ_s stand for the sensor signal full scale and the oversampling clock, respectively. Basically, the principle of operation follows the behavior of a low-pass first-order single-bit CT ΔΣM loop [25]. Firstly, the chemical input signal causes the change I_{in} in the sensor current, which is compared with the prediction I_{sens} coming from the feedback DAC. The resulting error current is then amplified and converted into voltage V_{rw} by the electrochemical sensor impedance itself, which is also in charge of shaping the quantization noise in frequency. The comparator computes the single-bit quantization of V_{rw} in q_{comp}, while the D-type flip-flop stage implements its sample and hold in q_{mod}. Finally, this output bit stream is fed back to the current DAC in order to update the signal prediction. As a result, q_{mod} is modulated by I_{in}, allowing the digital amperometric read-out of the chemical sensing signal. The potentiostat operation is obtained by the negative feedback of the ΔΣM loop, which ensures V_{rw} is biased close to the wanted DC potential V_{ref}, and the high input impedance of the comparator prevents from any current flowing through the reference microelectrode. Due to the intrinsic Class-A operation of the electrochemical sensor, signal full scale swing is maximized when:

$$I_{FS} = \frac{V_{ref}}{R_{ctw}} \tag{1}$$

From the signal processing viewpoint, the equivalent model of the proposed ΔΣM is depicted in Figure 3(b), where the noise shaping time-constant of the electrochemical lossy integrator is given by:

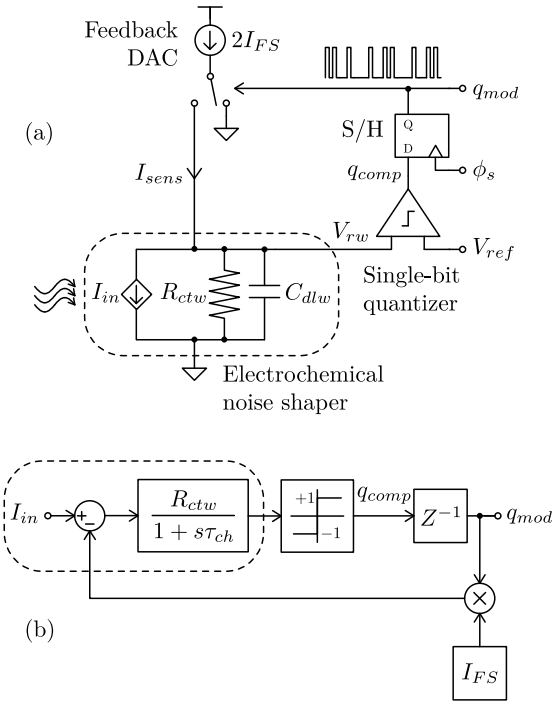

Figure 3. Electrical (a) and signal processing (b) models of the ΔΣM proposed for the potentiostat operation and amperometric digital read-out of electrochemical sensors.

$$\tau_{ch} = R_{ctw} C_{dlw} \tag{2}$$

Since the electrochemical bandwidth of the sensor is usually very limited, with typical τ_{ch} values in the 0.1s range, a large oversampling ratio (OSR) can be already obtained with a clock frequency f_s as low as few kHz. Combining this high OSR with the first-order noise shaping, theoretical signal-to-quantization-noise ratio (SQNR) values exceeding 10-bit could be easily achieved. However, two major issues arise in practice from the electrochemical ΔΣM architecture of Figure 3(b).

The first unwanted effect is the presence of extra tones at the modulated output under harmonic stimulus, which is caused by the well-known correlation between quantization error and signal in first-order noise shaping. A numerical example of this effect is shown in Figure 4(a) for a typical electrochemical sensor. In order to minimize this tonal response without increasing the order of the ΔΣM, the introduction of dithering is chosen. In general, the effectiveness of dithering against tones depends on the location of the injection inside the ΔΣM loop and the statistical properties of the dithering source [26], returning different circuit overheads for each case. Here, the thermal noise of the feedback DAC circuit is proposed to be reused as the electrical source for dithering, thus no extra blocks are added to the minimalist architecture of Figure 3(a). In practice, the minimum noise specification for the $2I_{FS}$ current source to ensure proper tonal suppression can be obtained from the behavioral simulation of Figure 3(b), like in the example of Figure 4(b).

The second undesired effect is the existence of signal dead zones in the DC transfer function of the ΔΣM due to the integrator losses of the electrochemical noise shaper [27], [28].

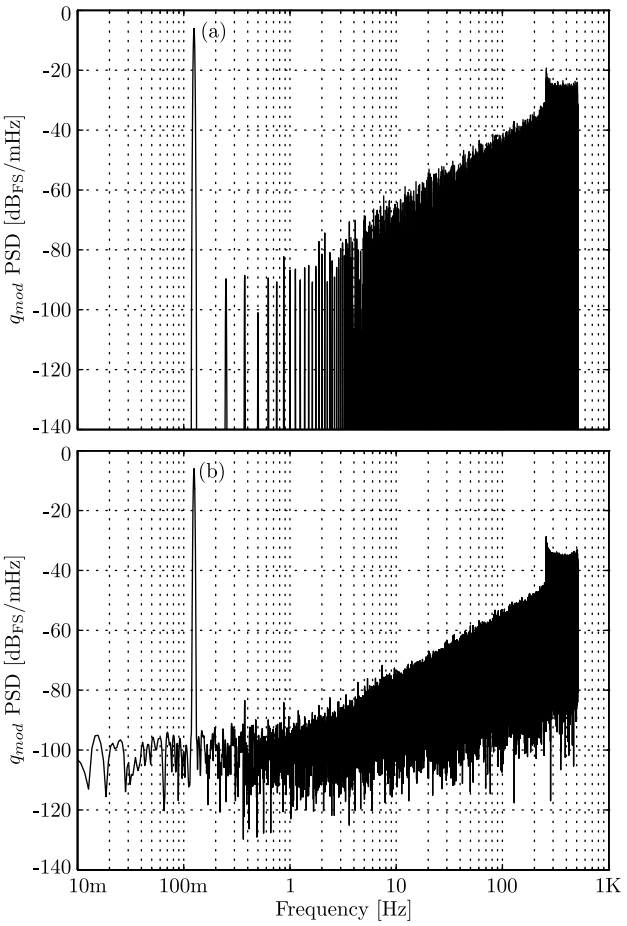

Figure 4. Example of behavioral harmonic simulation of the ΔΣM model of Figure 3(b) without (a) and with (b) DAC white noise dithering at −80dB$_{FS}$ for R_{ctw}=500kΩ, τ_{ch}=0.16s, V_{ref}=1V, I_{FS}=2μA, f_s=1024Hz (OSR=512) and half full scale input at 0.125Hz.

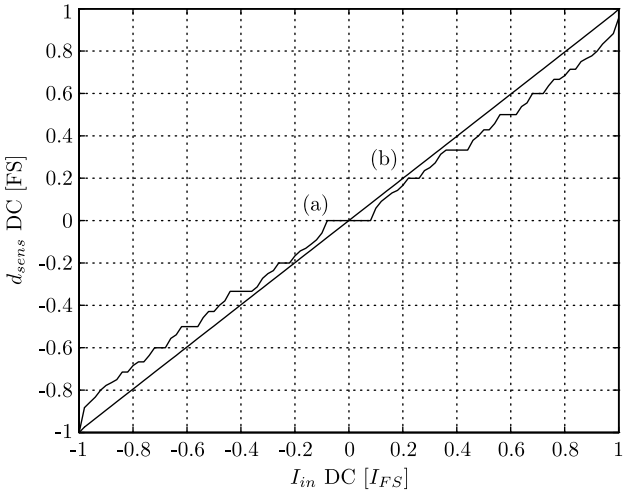

Figure 5. Example of behavioral DC simulation of the ΔΣM model of Figure 3(b) at f_s=32Hz (OSR=16) (a) and f_s=1024Hz (OSR=512) (b) for R_{ctw}=500kΩ, τ_{ch}=0.16s, V_{ref}=1V and I_{FS}=2μA.

The resulting fractal staircase can be clearly seen in Figure 5(a) for a practical electrochemical sensor example. Since the size of these dead zones depends on the amount of losses seen under discrete time operation, the CT leaking effect can be strongly attenuated by increasing the OSR of the ΔΣM, as illustrated in Figure 5(b).

IV. Low-Power All-MOS Delta-Sigma Modulator Circuits

The only two analog circuit blocks required for the electrochemical ΔΣM architecture proposed in Figure 3(a) are the single-bit quantizer and the feedback current DAC.

Figure 6(a) shows the comparator selected for the all-MOS implementation of the single-bit quantizer. A latched solution is preferred to achieve null DC power consumption. The quantization process involves two phases: pre-setting the circuit to a symmetrical bias point (ϕ_s=1), and the voltage comparison itself (ϕ_s=0). During this second phase, the local positive feedback network M5-M6 allows fast digital transitions at the output q_{comp}. Thanks to the single-bit configuration, technology mismatching can be neglected here, as it is equivalent to a static offset voltage added to V_{ref} without any effect on signal distortion. From the electrochemical viewpoint, as long as V_{ref} is higher than the redox potential, the sensitivity of the amperometric reading to this voltage level is low, allowing offset values as large as ±10mV.

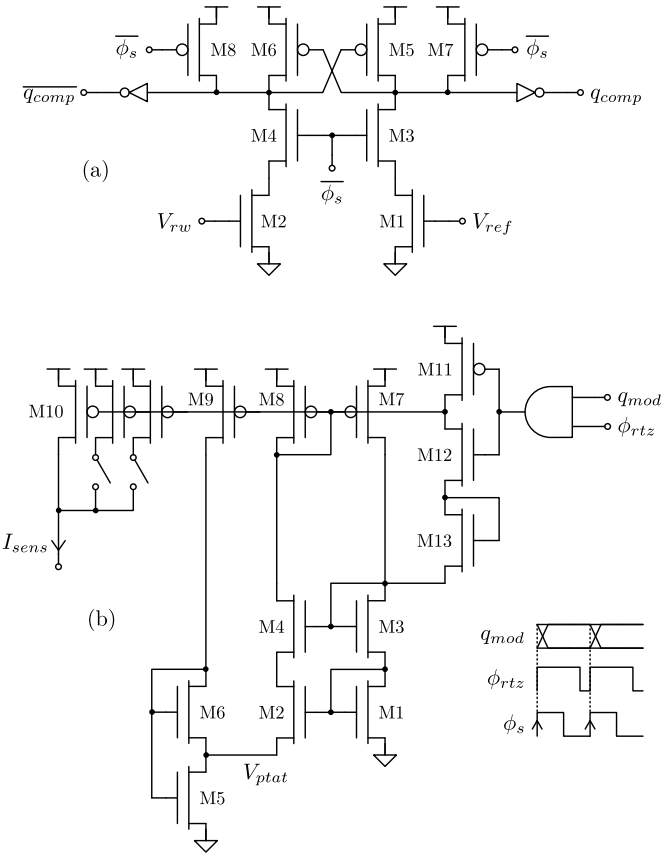

Figure 6. Low-power all-MOS circuits for the single-bit quantizer (a) and feedback DAC (b) blocks of Figure 3(a). Bulk terminals are connected to their corresponding supply voltage.

Concerning the single-bit feedback DAC, the proposed all-MOS current source is shown in Figure 6(b). The core of the circuit M1-M9 is based on a previous work from these

authors [29]. The principle of operation can be explained in two steps. Firstly, the matched pair M1-M2 operating in weak inversion saturation combined with the feedback current mirror M7-M8 generates the proportional to absolute temperature (PTAT) voltage reference:

$$V_{ptat} = U_t \ln P \qquad P = \frac{(W/L)_2}{(W/L)_1}\frac{(W/L)_7}{(W/L)_8} \tag{3}$$

where U_t is the well-known thermal potential, while W/L stands for the aspect ratio of each MOS transistor. Secondly, the equivalent I_{FS} of Figure 3(a) is obtained through the nonlinear load M5-M6 attached to V_{ptat}. Assuming strong inversion saturation and linear mode for M6 and M5 devices, respectively, the resulting full scale current reference:

$$I_{FS} = \frac{Q}{8}\left[\frac{\ln P}{M+1}\left(\sqrt{\frac{M}{N}} + \sqrt{\frac{M}{N}+M+1}\right)\right]^2 \left(\frac{W}{L}\right)_5 I_S$$
$$Q = \frac{(W/L)_{10}}{(W/L)_8} \qquad M = \frac{(W/L)_9}{(W/L)_8} \qquad N = \frac{(W/L)_6}{(W/L)_5} \tag{4}$$

is proportional to the specific current [30]:

$$I_S = 2n\beta U_t^2 \tag{5}$$

where n and β stand for the slope factor and the transfer parameter of the target CMOS technology, respectively. Cascode devices M3-M4 are included in Figure 6(b) to avoid channel length modulation at the wide translinear pair M1-M2. The resulting I_{FS} can be easily adapted to different electrochemical sensors by scaling the multiplicity of transistor M10. As for the q_{mod} control of the output current I_{sens}, the power-on/off switching mechanism M11-M13 is introduced instead of the current steering procedure depicted in Figure 3(a). In this way, the long-term charge trapped in the oxide interface of the MOS transistors is periodically reset to reduce flicker noise contributions [31], [32]. For this purpose, M11-M12 is operated as a digital inverter, while M13 ensures the proper start-up of the overall reference circuit at each transition. Finally, the feedback control bit stream q_{mod} is digitally masked by the return-to-zero (RTZ) clock ϕ_{rtz} to avoid the typical waveform asymmetry issues of CT $\Delta\Sigma$Ms [23]. Like in the case of the single-bit quantizer circuit of Figure 6(a), the effect of technology mismatching can be also neglected here.

V. Application to Low-Cost Smart Electrochemical Sensors

The low-power all-MOS potentiostatic $\Delta\Sigma$M proposed in previous sections is applied to the development of the fully integrated smart electrochemical sensor of Figure 7. The target technology is the low-cost 2.5μm 1M CMOS process (CNM25) from IMB-CNM(CSIC) combined with Au post-processing at wafer level for the integration of the electrochemical sensor microelectrodes. This in-house CMOS post-processing involves standard lithographic techniques for the sputter deposition of Ti(15nm) and Au(150nm) thin films and for the sensor microelectrodes patterning by lift-off.

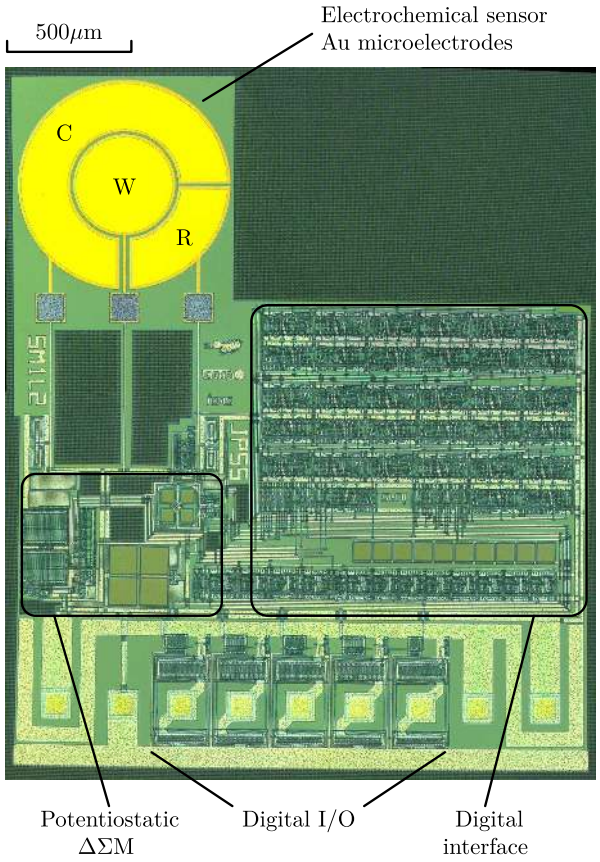

Figure 7. Microscope photograph of the complete smart electrochemical sensor in CNM25 with Au post-processing. Integrated circuit size is 2.3mm×2.8mm (6.4mm^2).

Concerning the electrochemical sensor layout, the working microelectrode diameter is 390μm, while the outer diameter of the reference and counter microelectrodes is 830μm with 30μm spacing between all of them. The electrical parameters of the sensor model are R_{ctw}=500kΩ and τ_{ch}=0.16s. As for the electrical part of the $\Delta\Sigma$M, the typical design parameters are V_{ref}=1V, I_{FS}=2μA and f_s=1024Hz (OSR=1024). From the integrated circuit photograph of Figure 7, it is clear that the potentiostatic $\Delta\Sigma$M does not introduce excessive area overhead compared to the electrochemical sensor alone. The purpose of the digital interface block is to incorporate the low-pass digital filtering of Figure 1(c) and to configure both I_{FS} and V_{ref}. Finally, electrostatic discharge (ESD) protections attached to the sensor reference and counter microelectrodes are also included in the same die.

VI. Experimental Results

This section reports measurements obtained from the smart electrochemical sensor of Figure 7.

A. Electrical Tests

In order to improve the observability of the potentiostatic $\Delta\Sigma$M proposed in Figure 3, electrical tests are applied to the integrated circuit of Figure 7 following the setup of Figure 8(a). In this case, the electrochemical sensor is emulated by external R_{ctw}=510kΩ and C_{dlw}=330nF discrete

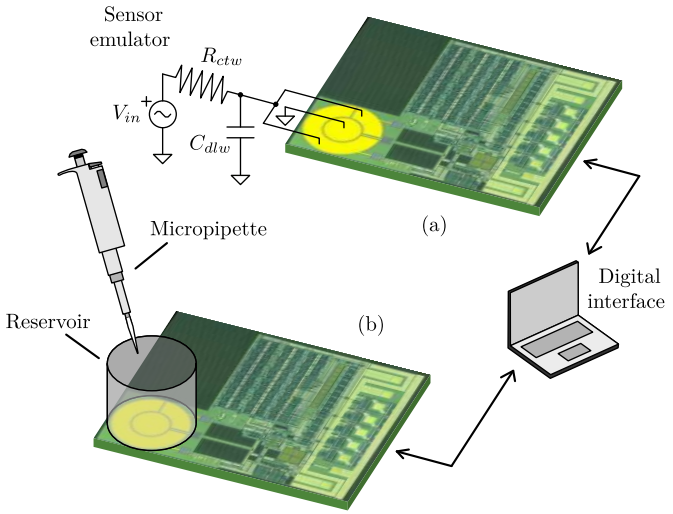

Figure 8. Laboratory setup for the electrical (a) and electrochemical (b) tests of the smart sensor of Figure 7.

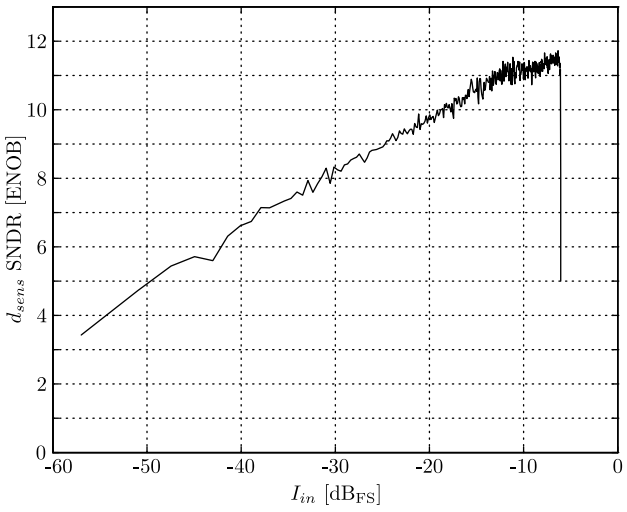

Figure 10. Experimental DC results following Figure 8(a) from the potentiostatic $\Delta\Sigma$M in Figure 7 for V_{ref}=1V, I_{FS}=2μA and f_s=1024Hz (OSR=256). Equivalent noise bandwidth is 2Hz.

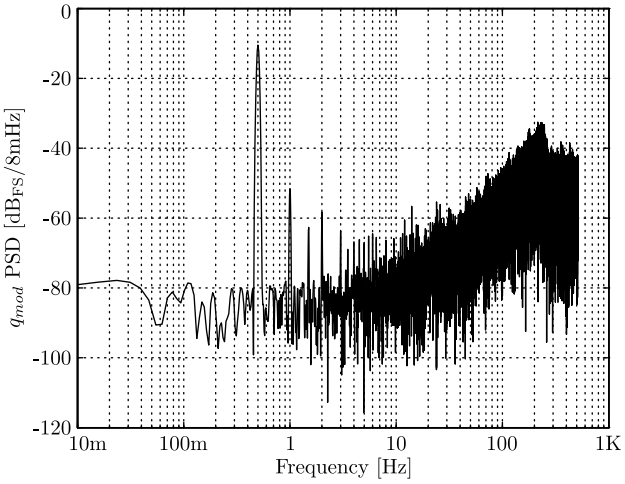

Figure 9. Experimental harmonic results following Figure 8(a) from the potentiostatic $\Delta\Sigma$M of Figure 7 for V_{ref}=1V, I_{FS}=2μA, f_s=1024Hz (OSR=512) and half full scale input at 0.5Hz.

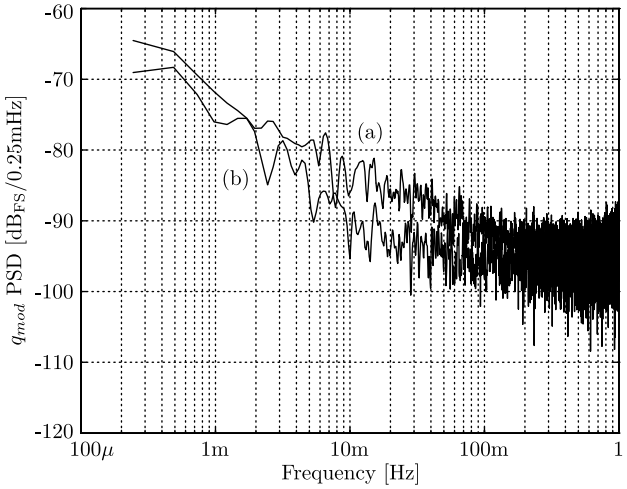

Figure 11. Experimental flicker noise results following Figure 8(a) from the potentiostatic $\Delta\Sigma$M in Figure 7 for V_{ref}=1V, I_{FS}=2μA and f_s=1024Hz (OSR=512) when the feedback DAC is under current steering (a) or power on/off (b) operation.

components together with Standford Research Systems DS360 voltage generator in the Thevenin configuration equivalent to the sensor model of Figure 2(c).

Figure 9 shows the response of the proposed potentiostatic $\Delta\Sigma$M under harmonic stimulus. Although the amount of thermal noise dithering coming from the feedback DAC should be increased in order to minimize signal distortion, the modulator returns a remarkable robustness against tonal generation even at amplitude levels close to full scale. Nevertheless, since chemical signals exhibit in practice very slow transitions, the quasi-static electrical characterization of the potentiostatic $\Delta\Sigma$M is preferred for our purposes. In this sense, the results reported in Figure 10 show a large enough dynamic range to not limit the overall resolution of the full electrochemical $\Delta\Sigma$M. Furthermore, statistical analysis on 9 die samples return dynamic range deviations below $\pm$0.5-bit.

Finally, the flicker noise reduction mechanism introduced in Section IV is also tested here, since the potentiostatic $\Delta\Sigma$M of Figure 7 can operate its feedback DAC following the current steering scheme of Figure 3(a) or the switched power on/off strategy of Figure 6(b). The comparative results of Figure 11 show that a flicker noise power reduction of around 3dB can be obtained by resetting the MOS devices of the DAC current source.

B. Electrochemical Tests

Ferrocyanide ion $[Fe(CN)_6]^{4-}$ is commonly accepted in electrochemistry as a standard compound to characterize amperometric sensors due to its electrochemical propoerties, like its high reversibility. At the appropriate potential of operation, Ferrocyanide ions are oxidized into Ferricyanide ions following:

$$[Fe(CN)_6]^{4-} \rightarrow [Fe(CN)_6]^{3-} + 1e^- \qquad (6)$$

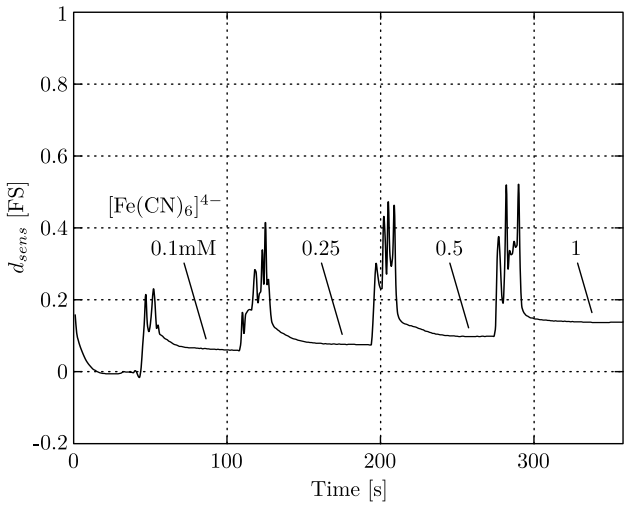

Figure 12. Experimental chronoamperogram from the smart electrochemical sensor of Figure 7 at different Ferrocyanide ion concentration levels in PBS pH=7 for V_{ref}=0.7V, I_{FS}=2μA and f_s=1024Hz (OSR=1024).

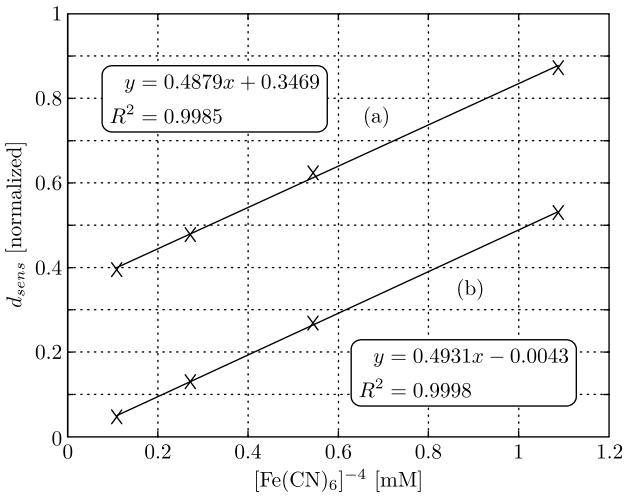

Figure 13. Experimental comparison of Ferrocyanide calibration curve in PBS pH=7 between the smart electrochemical sensor of Figure 7 for V_{ref}=0.7V, I_{FS}=2μA and f_s=1024Hz (OSR=1024) (a), and the same Au microelectrode structure in conjunction with external CH Instruments 1030B Multipotentiostat (b).

For our purposes, the amperometric measurements of Ferrocyanide oxidation are performed in a 10μl reservoir filled with Ferrocyanide dissolved in Phosphate buffer solution (PBS) at pH=7 following the setup of Figure 8(b). Also, the potentiostatic voltage of the smart sensor is digitally programmed to V_{ref}=0.7V, which is high enough to oxidize Ferrocyanide ions as described in (6).

Figure 12 shows the transient response obtained from the complete smart electrochemical sensor of Figure 7 when Ferrocyanide ion concentration is swept from 0.1mM to 1mM in discrete time steps. The electrochemical time constant τ_{ch} observed in the same figure is similar to the electrical model $R_{ctw}C_{dlw}$ used during the CMOS design of Section V and for the external sensor emulator in the electrical tests of Section VI-A. The smart sensor shows a remarkable linearity below 1mM, with the linear regression d_{sens}=0.076($\pm$0.009)[Fe(CN)$_6$]$^{4-}$+0.04($\pm$0.01) for 6 die samples (n=6). Concerning reproducibility, the residual standard deviation (RSD) of the slope returned by these results is less than 15%.

In order to qualify the performance of the smart electrochemical sensor of Figure 7, its response is compared to the same Au microelectrode structure connected to an external CH Instruments 1030B Multipotentiostat measurement equipment. Figure 13 reports the results obtained from this comparison after normalization. Both responses are clearly comparable in performance, showing coefficients of determination (R^2) for their slopes larger than 0.99, which is in general linear enough for chemical sensing applications. Finally, the main results of the fully integrated smart sensor tests are summarized in Table I.

Table I
SMART ELECTROCHEMICAL SENSOR RESULTS

Parameter	Value	Units
Full scale range	2 to 32	μA
Potential range	0 to 5	V
Sampling frequency	1	kHz
Oversampling ratio	$\geq$256	
Electrical dynamic range	>10	ENOB
Residual standard deviation (n=6)	<15	%
Coefficient of determination (R^2)	0.9985	
Supply voltage	5	V
Power consumption at 2μA$_{FS}$	25	μW
Die size	2.3×2.8	mm^2

VII. CONCLUSIONS

A low-power all-MOS delta-sigma ADC has been presented for the potentiostatic biasing and amperometric read-out of integrated electrochemical sensors. The proposed architecture exploits the dynamic properties of the sensor itself to implement a continuous-time mixed electrochemical delta-sigma modulator. Thanks to this circuit strategy, the resulting ADC only requires minimalist analog circuits and the complete smart sensor can be integrated in purely digital CMOS technologies. In order to proof the validity of the proposed converter, a 25-μW smart electrochemical sensor demonstrator with all-digital and configurable interface is developed in low-cost 1M CMOS technology with Au post-processing for the integration of the sensor microelectrodes. Experimental results report electrical dynamic range values exceeding 10-bit, while electrochemical figures exhibit linearity levels close to R^2=0.999 combined with RSD<15% in terms of reproducibility. A comparative test with commercial potentiostat equipment is also included to qualify the performance of the proposed ADC.

ACKNOWLEDGMENT

This work has been partially funded by the Catrene Pasteur (CT-204) project from the European Union.

REFERENCES

[1] G. Chen, S. Hanson, D. Blaauw, and D. Sylvester, "Circuit Design Advances for Wireless Sensing Applications," *Proc. IEEE*, vol. 98, no. 11, pp. 1808–1827, Nov 2010.

[2] S. Lee, L. Yan, T. Roh, S. Hong, and H.-J. Yoo, "A 75μW Real-Time Scalable Body Area Network Controller and a 25μW ExG Sensor IC for Compact Sleep Monitoring Applications," *IEEE J. Solid-State Circuits*, vol. 47, no. 1, pp. 323–334, Jan 2012.

[3] W.-D. Huang, S. Deb, Y.-S. Seo, S. Rao, M. Chiao, and J. Chiao, "A Passive Radio-Frequency pH-Sensing Tag for Wireless Food-Quality Monitoring," *IEEE Sensors J.*, vol. 12, no. 3, pp. 487–495, Mar 2012.

[4] K. Y. Inoue, M. Matsudaira, R. Kubo, M. Nakano, S. Yoshida, S. Matsuzaki, A. Suda, R. Kunikata, T. Kimura, R. Tsurumi, T. Shioya, K. Ino, H. Shiku, S. Satoh, M. Esashi, and T. Matsue, "LSI-Based Amperometric Sensor for Bio-Imaging and Multi-Point Biosensing," *RSC Lab on a Chip*, vol. 12, no. 18, pp. 3481–3490, 2012.

[5] J. Croce, RobertA., S. Vaddiraju, J. Kondo, Y. Wang, L. Zuo, K. Zhu, S. Islam, D. Burgess, F. Papadimitrakopoulos, and F. Jain, "A Miniaturized Transcutaneous System for Continuous Glucose Monitoring," *Springer Biomedical Microdevices*, vol. 15, no. 1, pp. 151–160, 2013.

[6] C. Yang, Y. Huang, B. Hassler, R. Worden, and A. Mason, "Amperometric Electrochemical Microsystem for a Miniaturized Protein Biosensor Array," *IEEE Trans. Biomed. Circuits Syst.*, vol. 3, no. 3, pp. 160–168, Jun 2009.

[7] L. Li, X. Liu, W. Qureshi, and A. Mason, "CMOS Amperometric Instrumentation and Packaging for Biosensor Array Applications," *IEEE Trans. Biomed. Circuits Syst.*, vol. 5, no. 5, pp. 439–448, Oct 2011.

[8] S. Martin, F. Gebara, T. Strong, and R. Brown, "A Fully Differential Potentiostat," *IEEE Sensors J.*, vol. 9, no. 2, pp. 135–142, Feb 2009.

[9] L. Fujcik, R. Prokop, J. Prasek, J. Hubalek, and R. Vrba, "New CMOS Potentiostat as ASIC for Several Electrochemical Microsensors Construction," *Emerald Microelectronics International*, vol. 27, no. 1, pp. 3–10, 2010.

[10] H. Narula and J. Harris, "A Time-Based VLSI Potentiostat for Ion Current Measurements," *IEEE Sensors J.*, vol. 6, no. 2, pp. 239–247, Apr 2006.

[11] S. Hasan, "Stability Analysis and Novel Compensation of a CMOS Current-Feedback Potentiostat Circuit for Electrochemical Sensors," *IEEE Sensors J.*, vol. 7, no. 5, pp. 814–824, May 2007.

[12] M. Stanacevic, K. Murari, A. Rege, G. Cauwenberghs, and N. Thakor, "VLSI Potentiostat Array With Oversampling Gain Modulation for Wide-Range Neurotransmitter Sensing," *IEEE Trans. Biomed. Circuits Syst.*, vol. 1, no. 1, pp. 63–72, Mar 2007.

[13] S. Ayers, K. Gillis, M. Lindau, and B. Minch, "Design of a CMOS Potentiostat Circuit for Electrochemical Detector Arrays," *IEEE Trans. Circuits Syst. I*, vol. 54, no. 4, pp. 736–744, Apr 2007.

[14] P. Levine, P. Gong, R. Levicky, and K. Shepard, "Active CMOS Sensor Array for Electrochemical Biomolecular Detection," *IEEE J. Solid-State Circuits*, vol. 43, no. 8, pp. 1859–1871, Aug 2008.

[15] M. Ahmadi and G. Jullien, "Current-Mirror-Based Potentiostats for Three-Electrode Amperometric Electrochemical Sensors," *IEEE Trans. Circuits Syst. I*, vol. 56, no. 7, pp. 1339–1348, Jul 2009.

[16] S. Hwang and S. Sonkusale, "CMOS VLSI Potentiostat for Portable Environmental Sensing Applications," *IEEE Sensors J.*, vol. 10, no. 4, pp. 820–821, Apr 2010.

[17] Y.-T. Liao, H. Yao, A. Lingley, B. Parviz, and B. Otis, "A 3μW CMOS Glucose Sensor for Wireless Contact-Lens Tear Glucose Monitoring," *IEEE J. Solid-State Circuits*, vol. 47, no. 1, pp. 335–344, Jan 2012.

[18] M. H. Nazari, H. Mazhab-Jafari, L. Leng, A. Guenther, and R. Genov, "CMOS Neurotransmitter Microarray: 96-Channel Integrated Potentiostat With On-Die Microsensors," *IEEE Trans. Biomed. Circuits Syst.*, 2012, accepted.

[19] R. Turner, D. Harrison, and H. Baltes, "A CMOS Potentiostat for Amperometric Chemical Sensors," *IEEE J. Solid-State Circuits*, vol. 22, no. 3, pp. 473–478, Mar 1987.

[20] K. C. Smith and A. Sedra, "The Current Conveyor - A New Circuit Building Block," *Proc. IEEE*, vol. 56, no. 1368–1369, pp. 1368–1369, Aug 1968.

[21] J. B. Allen and R. F. Larry, *Electrochemical Methods: Fundamentals and Applications*, Department of Chemistry and Biochemistry University of Texas at Austin, Ed. John Wiley & Sons, Inc, 2001.

[22] F. Heer, M. Keller, G. Yu, J. Janata, M. Josowicz, and A. Hierlemann, "CMOS Electro-Chemical DNA-Detection Array with On-Chip ADC," in *Proceedings of the International Solid-State Circuits Conference*. IEEE, Feb 2008, pp. 168–604.

[23] R. W. Adams, "Design and Implementation of an Audio 18-Bit Analog-to-Digital Converter Using Oversampling Techniques," *Journal of Audio Engineering Society*, vol. 34, pp. 153–166, Mar 1986.

[24] A. J. Bard and L. R. Faulkner, *Electrochemical Methods: Fundamentals and Applications*. John Wiley & Sons, Jan 2000.

[25] R. Schreier and G. Temes, *Understanding Delta-Sigma Data Converters*, IEEE Press, Ed. John Wiley & Sons, 2004.

[26] G. Taylor and I. Galton, "A Mostly-Digital Variable-Rate Continuous-Time Delta-Sigma Modulator ADC," *IEEE J. Solid-State Circuits*, vol. 45, no. 12, pp. 2634–2646, Dec 2010.

[27] O. Feely and L. Chua, "The Effect of Integrator Leak in $\Sigma - \Delta$ Modulation," *IEEE Trans. Circuits Syst.*, vol. 38, no. 11, pp. 1293–1305, Nov 1991.

[28] S. Park and R. Gray, "Sigma-Delta Modulation with Leaky Integration and Constant Input ," *IEEE Trans. Inf. Theory*, vol. 38, no. 4, pp. 1512–1529, Sep 1992.

[29] F. Serra-Graells and J. L. Huertas, "Sub-1V CMOS Proportional-to-Absolute-Temperature References," *IEEE J. Solid-State Circuits*, vol. 38, no. 1, pp. 84–88, Jan 2003.

[30] C. C. Enz, F. Krummenacher, and E. A. Vittoz, "An Analytical MOS Transistor Model Valid in All Regions of Operation and Dedicated to Low-Voltage and Low-Current Applications," *Journal of Analog Integrated Circuits and Signal Processing, Kluwer Academic Publishers*, vol. 8, no. 1, pp. 83–114, 1995.

[31] E. A. M. Klumperink, S. L. J. Gierkink, A. P. van der Wel, and B. Nauta, "Reducing MOSFET $1/f$ Noise and Power Consumption by Switching Biasing," *IEEE J. Solid-State Circuits*, vol. 35, no. 7, p. 994, Jul 2000.

[32] D. Siprak, M. Tiebout, N. Zanolla, P. Baumgartner, and C. Fiegna, "Noise Reduction in CMOS Circuits Through Switched Gate and Forward Substrate Bias," *IEEE J. Solid-State Circuits*, vol. 44, no. 7, pp. 1959–1967, Jul 2009.